Aalborg Universitet

AALBORG UNIVERSITY
DENMARK

Accessing a Forbidden Disordered State of a Zeolitic Imidazolate Framework with Higher Stiffness and Toughness through Irradiation

Du, Tao; Sørensen, Søren Strandskov; Zhou, Qi; Bauchy, Mathieu; Smedskjær, Morten Mattrup

Accessing a Forbidden Disordered State of a Zeolitic Imidazolate Framework with Higher Stiffness and Toughness through Irradiation

Tao Du[1], Søren S. Sørensen[1], Qi Zhou[2], Mathieu Bauchy[2], Morten M. Smedskjaer[1,*]

[1]*Department of Chemistry and Bioscience, Aalborg University, Aalborg East 9220, Denmark*
[2]*Physics of AmoRphous and Inorganic Solids Laboratory (PARISlab), Department of Civil and Environmental Engineering, University of California, Los Angeles, CA 90095, USA*
* Corresponding author. e-mail: mos@bio.aau.dk

Abstract

Metal-organic frameworks (MOFs) with nanoscale porosity have numerous potential applications, for example within catalysis, shock absorption, ion transportation, gas sorption and separation. Recently, the disordered state of MOFs has also attracted significant attention, since some MOF crystals can melt and be quenched into bulk glasses, as first discovered for zeolitic imidazolate frameworks (ZIFs, a subset of MOFs). Another potential route to disorder in MOFs – that so far remains unexplored – is irradiation, e.g., silicate minerals are well-known to rearrange into a disordered state upon irradiation. Here, we investigate the structural disordering of both ZIF-4 crystals and glasses under irradiation using reactive molecular dynamics simulations. Our results show that the two phases converge toward a new "forbidden" disordered state that is not accessible through any thermal path. The evolution of the structure upon irradiation allows us to establish a relationship between structural disorder and mechanical properties to explain why the irradiated ZIF-4 state is both stiffer and tougher than that of both the parent ZIF-4 crystal and glass.

1. Introduction

Metal-organic frameworks (MOFs) are porous hybrid materials, consisting of metal ion-nodes connected by organic linkers. The presence of nanoscale porosity makes MOFs suitable for various applications, such as gas sorption and separation[1], shock absorbtion[2], catalysis[3], and ion transportation[4]. Recently, it has been found that a subset of MOFs, including a variety of zeolitic imidazolate frameworks (ZIFs), can melt before they thermally decompose and then be quenched to a disordered glass state[5,6]. Such MOF glasses can be easily formed in bulk pieces, which does not only overcome the shortcomings of crystalline MOF powders, but the glasses also display interesting features such as high transparency[7], luminescence[8], and in some cases maintain some level of the porosity of their parent crystals[9,10]. ZIF glasses are, to some extent, structurally analogous to silica glasses due to the presence of tetrahedral metal ions (e.g., Zn and Co, denoted as M) connected by imidazole (Im, $C_3N_2H_3$)-based ligands with an average M-Im-M angle of 145°[11].

The first ZIF to be melt-quenched to a glassy state was ZIF-4 ($Zn[Im]_2$). It has a relatively high glass-forming ability[5] and various experimental and simulation studies have since then been conducted on this system, including structural studies of its crystalline, liquid, and glass states, as well as the melting mechanism[6,12–14]. Besides glass formation through standard melt-quenching, crystalline ZIFs can also be transformed into an amorphous (disordered) state by mechanical treatment such as pressurization[15] or ball-milling[16]. Note that, although "glasses" and "amorphous" are both used to describe noncrystalline solids, here, we used the classification introduced by Gupta[17]. Namely, glass exhibits a glass transition and tends to relax toward the supercooled liquid state upon heating, while an amorphous solid tends to relax directly toward the stable crystalline state—which indicates that glasses and amorphous solids essentially lie in two distinct regions of the energy landscape. Besides melt-quenching and ball-milling, it is also possible to access the disordered state of various inorganic compounds through sol-gel synthesis, irradiation, and vapor deposition[18]. For example, irradiation induces the formation and accumulation of defects in the atomic structure of crystal materials, which eventually leads to a disordered atomic structure. In the case of α-quartz, the irradiation-induced disordering leads to the formation of a "forbidden state," i.e., a state that is inaccessible through simply thermal treatment such as heating and cooling[19]. Based on the concept of "defective by design," such disordering can promote the amorphous-to-glassy[20] and brittle-to-ductile[21] transition of silica, since the irradiation process leads to enhanced local atomic self-organization.

Identifying routes to improve the mechanical properties of disordered MOFs is important, since they face challenges related to the synthesis of large, defect-free monoliths as well as low fracture toughness[22]. Inspired by the previous work on the structural analogue of silica, we here seek to understand the changes in structure and mechanical properties of ZIF-4 upon irradiation.

In detail, we investigate the influence of irradiation on the structure and mechanical properties of both crystalline and glassy states of ZIF-4 by means of reactive molecular dynamics (MD) simulations. The irradiation-induced structural changes are evaluated on both short- and medium-range order length scales, including coordination number, pair distribution function, ring statistics, and network topology. The mechanical properties of the irradiated samples are analyzed in terms of elastic modulus and fracture toughness. Based on these results, we find that despite the significant differences in the initial structure of crystalline and glassy ZIF-4, the two states converge toward a common disordered state in terms of both structure and mechanical properties upon irradiation. Specifically, we reveal the existence of a volume reduction and breakdown of imidazole rings upon irradiation, which lead to a stiffer and tougher material. This suggests that access to forbidden states of MOF materials by tailoring their extent and type of disorder can be used to control their properties—which offers an additional degree of freedom besides thermal treatments and chemical composition.

2. Methods

2.1 Reactive MD simulations

The reactive (ReaxFF) MD simulations were carried out using the GPU-accelerated LAMMPS package. The visualization of the snapshots was achieved using the OVITO package[23]. The previously validated ReaxFF potential from Ref.[24] was adopted to describe the interatomic interactions of ZIF-4. ReaxFF is a bond order-based potential, which can (i) account for charge transfers, (ii) handle the breakage and formation of chemical bonds, and (iii) adapt the interatomic forcefield to the local environment of each atom. These features make ReaxFF an ideal forcefield to properly account for the formation of bulk or surface defects upon vitrification, irradiation, or fracture.

2.2 Simulation of melt-quenched glass

First, we simulated a ZIF-4 glass using the conventional melt-quenching method following the procedure from Ref.[24,25]. The initial configuration of the ZIF-4 crystal was obtained from the Cambridge Structural Database (CSD)[26] and then this structure was duplicated into a $4 \times 4 \times 4$ supercell (17408 atoms) to improve the statistics. This initial structure was subjected to an energy minimization process, followed by a relaxation for 7.5 ps at 10 K and 1 atm using a Berendsen thermostat[27]. The system was then heated to 300 K in 1.25 ps and further equilibrated at 300 K and 1 atm for 12.5 ps in the *NPT* ensemble with a Nosé–Hoover thermostat/barostat[28]. The structure was further heated to 1500 K within 50 ps, which is long enough to ensure that the structure is fully melted and has lost the memory of its initial configuration. The melt was subsequently cooled to 300 K at 24 K/ps to achieve a glassy state. Afterwards, the glassy structure was equilibrated at 300 K and 1 atm for 12.5 ps. A final run of 6.25 ps was conducted for statistical averaging of thermodynamic and structural properties. During the melt-quenching

3

simulation, the timestep for the motion integration was set to 0.25 fs.

2.3 Simulation of irradiation process

Both ZIF-4 crystal and glass samples were then subjected to an irradiation simulation following a well-established methodology as described in Refs.[19–21,29]. The irradiation simulation was achieved by initiating a series of displacement cascades, in which an atom was randomly selected to empower a kinetic energy of 100 eV with a random direction. Since MOF materials are more sensitive to irradiation than silica[30,31] due to the weaker Zn-N coordination bonds, the selected energy value is much lower than the typical value of 600 eV used previously in the irradiation simulation of silica. The selected atom known as the primary knock-on atom (PKA) acted as a projectile and collided with the neighboring atoms in the structure, thereby resulting in a ballistic cascade. The impacted zone around the PKA was defined as a spherical region with radius of 10 Å. To avoid any spurious effect of the thermostat on the dynamics of the impacted zone during the collision, the dynamics of the atoms inside the impacted zone were described in the *NVE* ensemble, while the rest of the atoms were equilibrated in the *NVT* ensemble at 300 K using a Berendsen thermostat[27]. Since the ballistic cascade contains high velocity atoms, a variable timestep was used to avoid any numerical instability. The maximum displacement allowed during a single timestep was set to 0.5 Å. The duration of cascade simulation lasted for 20 ps, which was found to be long enough for the system convergence of the thermodynamic properties (i.e., temperature, potential energy, and pressure), thereby indicating that the PKA had come to rest. Subsequently, the system was further equilibrated for 5 ps in the *NPT* ensemble at 300 K and zero pressure with a constant time step of 0.25 fs, which aims to adjust the configuration and volume of the system upon irradiation. The above process was repeated with different PKAs until the system exhibited a saturation in terms of energy, density, and structural features. The deposited energy of irradiation (as plotted in the figures) is defined as the cumulative empowered kinetic energy resulting from all the previous collisions averaged by the total number of atoms, i.e., each irradiation cycle will empower the system with a deposited energy of 100 eV / 17408 atoms = 0.00574 eV/atom.

2.4 Structure analysis of glasses

The structure of the ZIF-4 crystal and glasses before and after irradiation were analyzed in terms of density, potential energy, coordination analysis, pair distribution function (PDF), neutron structure factor (S(Q)), pore size distribution, ring statistics, and persistence diagrams. The PDFs represent the probability of finding a pair of atoms separated by a certain distance. The coordination number of Zn atoms was calculated using a cutoff of 2.8 Å, which corresponds to the minima after the first peak in the Zn-N pair distribution function. S(Q) was calculated through the Fourier transformation of the PDF using the Faber-Ziman formalism[32] as described in Ref.[33]. Pore structure analysis was performed using the Zeo++ software[34,35],

which relies on the algorithm of Voronoi decomposition to distinguish between the accessible and inaccessible volume/surface with a given spherical probe. This method has been extensively used in characterizing the pore structure within simulated MOF materials[24,36,37]. Due to the poor connectivity between pore pockets in the glassy and irradiated ZIF-4 states, we used a probe size of 0.01Å (as adopted from Ref.[24]) to calculate the pore size distribution. Finally, the number of imidazole rings was calculated using the RINGS package[38], where the imidazole rings are connected by 3 C and 2 N atoms.

To better characterize and understand the structural changes at medium-range order (MRO) length scales, we used persistent homology, which is an emerging topological data analysis tool to quantify (hidden) structural features in disordered materials that are not only due to chemical bonding but also spatial proximity[39]. Persistent homology has been extensively used to analyze the topological features of high-dimensional data across multiple scales[40,41]. When considering the atomic configuration of materials as a point cloud data set, the hierarchical structural features can be retrieved at different scales. In the case of disordered materials, persistent homology has demonstrated several advantages in understanding the MRO structure in different systems including oxide[39,42,43] and metallic[39,44] glasses, as well as glass structure altered by densification[42,43] or chemical replacement[45]. Here, we performed persistent homology analyses by calculating the so-called persistence diagrams of the different ZIF-4 structures using the packages of Diode[46] and Dionysus 2[47]. The procedure for obtaining the persistence diagram followed that in Ref.[39,48]. The atomic radius of each element was defined following the approach in Ref.[39]. Specifically, we obtained radii of r_C=0.715Å, r_H=0.395Å, r_N=0.625Å, and r_{Zn}=1.575Å.

2.5 Fracture simulations

The fracture behaviors of crystalline and glassy ZIF-4 influenced by irradiation were estimated by calculating the fracture toughness. This was done following the method of Brochard *et al.*[49], which is based on the energetic formulation of fracture mechanics without any assumptions of the fracture behavior of the material, namely, it can be applied in both brittle and ductile systems.[50–52] We first replicated the samples into 2 × 2 × 1 supercells of 69,632 atoms to minimize the size effect, and then manually inserted a sharp precrack, which is expected to appear naturally during cooling. The precrack was introduced by removing the atoms in an ellipsoidal cylinder with length of 48 Å and height of 6 Å at the center of the simulation box. Before applying stress, the precracked structures were equilibrated in the *NPT* ensemble at 300 K and zero pressure for 100 ps, which was found to be long enough for the new systems to converge their potential energy.[22] Afterwards, the precracked structures were subjected to uniaxial tensile loading by continuously elongation of the simulation box along the *x*-direction at a strain rate of 5 × 10⁸ s⁻¹, while the other two directions were free to deform by being

maintained at a zero pressure state. During the tensile process, the strain and corresponding stress in the loading direction were recorded until full fracture, i.e., stress decreased to zero.

Based on the stress-strain curve, the Young's modulus (E) was determined as the slope of the stress-strain curve in the low strain region ($\varepsilon < 0.05$) through linear regression. Then, the critical energy release rate (G_c), under the assumption of elongation in the x-direction, was calculated by integrating the stress-strain curve until fracture,

$$G_C = \frac{L_x L_y L_z}{\Delta A} \int_0^{\varepsilon_{xx}^f} \sigma_{xx} d\varepsilon_{xx},\tag{1}$$

where L is the dimension of the simulation box along the three directions, ΔA is the newly formed surface area created by fracture, ε_{xx}^f is the strain in the x-direction when fully fractures, σ_{xx} and ε_{xx} are the recorded stress and strain, respectively. Fracture toughness K_{Ic} was then estimated by the Irwin formula (where γ is assumed to be $G_c/2$),

$$K_{Ic} = \sqrt{2\gamma E},\tag{2}$$

where E is the Young's modulus.

3. Results and discussion

We first prepare simulated ZIF-4 glasses by heating and subsequent cooling the ZIF-4 crystal structure. The unit cell structure of crystalline ZIF-4 is shown in Fig. 1a, highlighting the periodically distributed tetrahedra (in grey) that consist of Zn atoms linked to four N atoms. The porosity of the structure is also evident with periodic channels surrounded by imidazole rings. When subjected to melt-quenching, the ZIF-4 structure becomes disordered with distorted tetrahedra and irregularly distributed pores (Fig. 1b). According to the melting mechanism proposed by Gaillac *et al.*[37], the undercoordination of Zn atoms act as nucleation sites for melting, and liquid ZIF-4 is dynamically equilibrated with the breaking and regeneration of Zn-N coordination bonds. This glass formation mechanism for ZIF-4 is summarized in Fig. 1c. The simulated total and partial pair distribution functions shown in Fig. 1d and S1 also demonstrate that the liquid ZIF-4 exhibits the most disordered structure compared to both the crystalline and glassy phases.
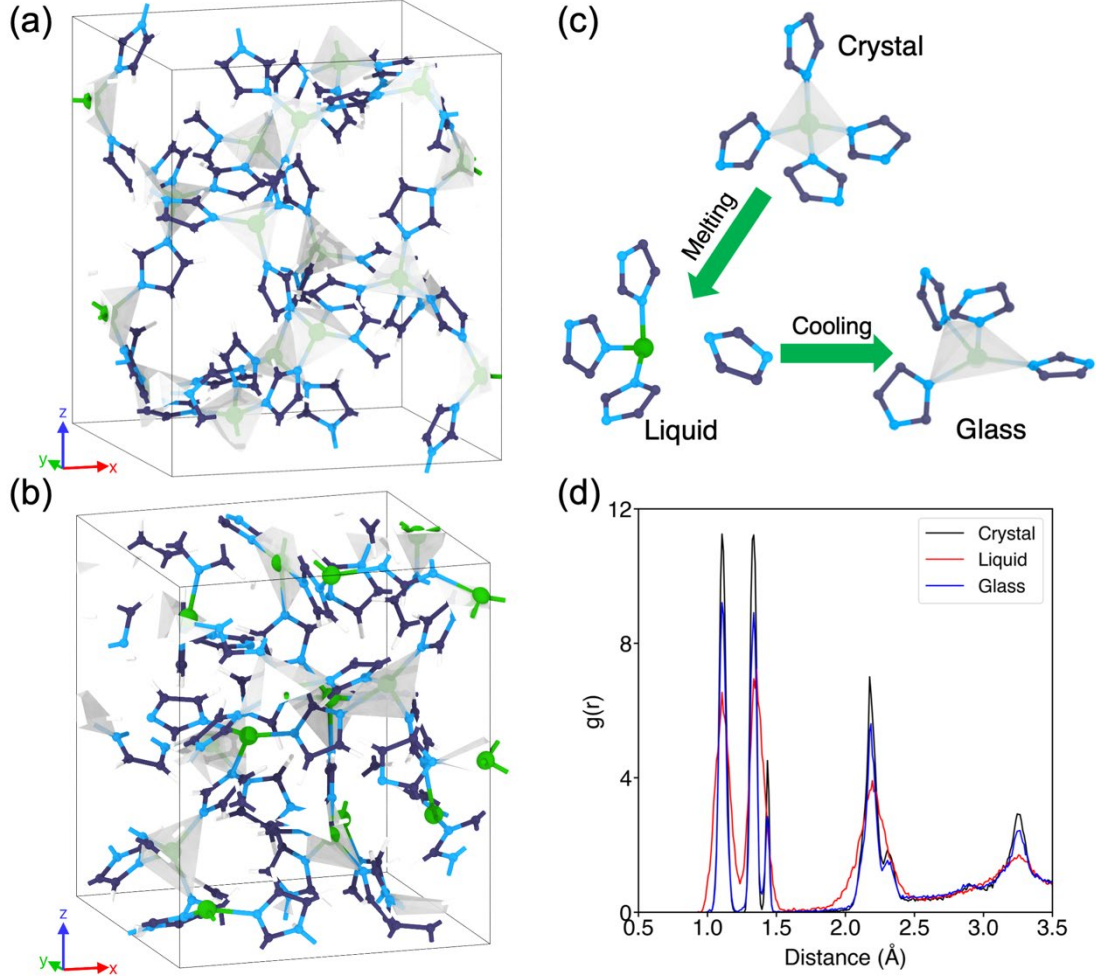
Fig. 1. Schematic of the unit cell structure of (a) ZIF-4 crystal (a = 15.395 Å, b = 15.3073 Å, c = 18.426Å, $\alpha = \beta = \gamma = 90°$) and (b) melt-quenched glass (a = 13.6847 Å, b = 13.6067 Å, c = 16.3789 Å, $\alpha = \beta = \gamma = 90°$). (c) Visualization of the changes in imidazolate groups of ZIF-4 upon vitrification. Zn, C, H and N are colored by green, grey, white, and light blue, respectively. (d) Pair distribution functions of ZIF-4 in crystalline, liquid, and glass states.

To examine the effects of irradiation on the ZIF-4 structures, we have calculated the coordination number (CN) of Zn, density, and the fraction of imidazole rings of the system as a function of the deposited energy upon the simulated irradiation. As shown in Fig. 2a, the densities of both crystalline and glassy ZIF-4 grow monotonically and eventually reach a constant value with an increase in the deposited energy. Interestingly, although glassy ZIF-4 exhibits a higher density than that of the crystalline phase due to the more porous structure of the latter, the densities of the irradiated states eventually both reach a value of around 1.77 g/cm³ after being subjected to a deposited energy of 2.5 eV/atom. Figure 2b shows that the CN of Zn decreases and then also reaches a constant value upon irradiation. The initial CNs of Zn in crystalline and glassy ZIF-4 were 4.0 and 3.8, respectively, which is consistent with the literature[24]. However, after an irradiation energy of 10 eV/atom has been deposited, the Zn-N

coordination number of both phases converge at around 3.2. Besides the decrease in the CN of Zn, we also observe a decomposition of the imidazole ring upon irradiation. As shown in Fig. 2c, the glassy ZIF-4 initially exhibits a similar number of imidazole rings as the crystalline counterpart, but in both systems the fraction of these rings gradually diminishes with an increase in the deposited energy. This decomposition may also be related to the change in the system's potential energy as shown in Fig. S2 in the Supporting Information. That is, the potential energy exhibits an initial increase and then decrease for both crystalline and glassy ZIF-4 systems upon irradiation, indicating that the structure of ZIF-4 keeps evolving despite the saturation in density and Zn-N structure upon irradiation. At the early stage of irradiation, since the system becomes denser, the average distance between the atoms decreases, which in turn increases the contribution of the Van Der Waals and Coulombic interactions to the potential energy. Additionally, although almost all imidazole rings have been decomposed as the irradiation energy saturates (Fig. 2c), the atomic chains from the decomposed imidazole rings can further be damaged by irradiation. This leads to the observed continuous decrease of the potential energy (Fig. S2).
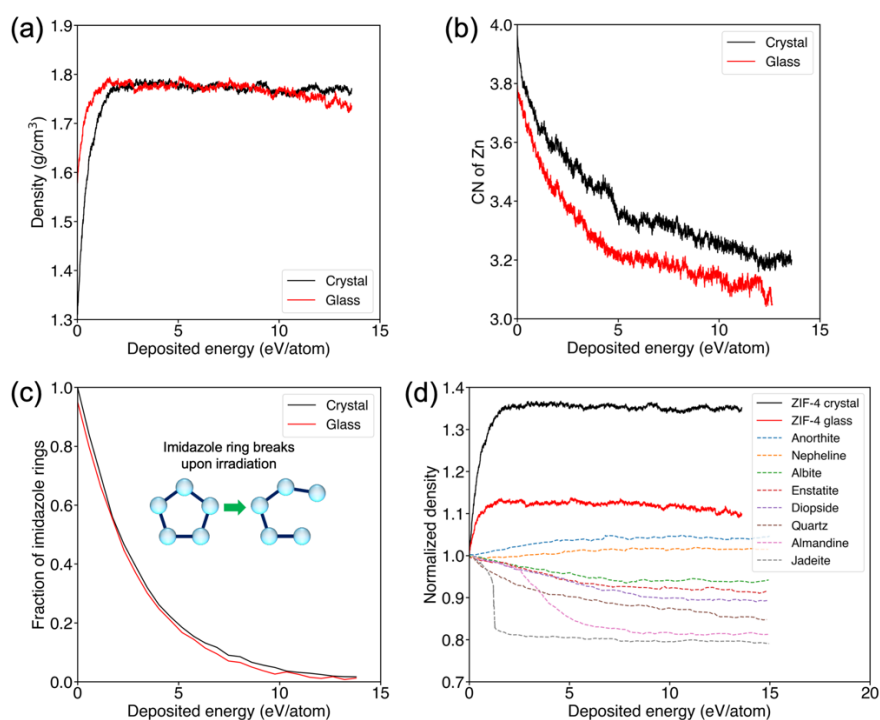
Fig. 2. Irradiation-induced evolution of (a) density, (b) average coordination number of Zn, and (c) Fraction of imidazole rings as a function of deposited energy for both crystalline and glassy ZIF-4 structures. (d) Normalized density change as a function of deposited energy in the present ZIFs as well as simulated silicate minerals. The silicate mineral data are taken from Ref.[29].

To compare the irradiation-induced changes in the structure of the ZIFs with that of other systems, we show the normalized density change as a function of the deposited energy in Fig.

2d. Unfortunately, there is a lack of comparable data for other MOF systems, while there are data on simulated silicate minerals that we can use for comparison. Most of the simulated silicate minerals from Ref.[29] exhibit swelling upon irradiation except for anorthite and nepheline, which have less open structure and exhibit a minor volume reduction. As such, compared with the silicate minerals, both crystalline and glassy ZIF-4s exhibit notably different behavior upon irradiation. First, both ZIF-4 phases exhibit a relatively large volumetric shrinkage rate, especially for crystalline ZIF-4. As reported in Ref.[29], the atomic structure changes in silicate minerals upon irradiation are similar to those of melt-quenching. However, for ZIF-4, irradiation can induce more significant structural rearrangements. Second, regarding the saturation of deposited energies, both crystalline and glassy ZIF-4s feature faster saturation speeds than others, namely, density reaches a plateau value at a relatively lower deposited energy. Given the projectile energy used here is significantly lower than that in the previous silicate simulations, the faster saturation upon irradiation is attributed to a lower atomic rigidity of ZIF-4, which controls the ability of the system to adjust its density upon an external stimulus. For instance, the N-Zn-N bond angle constraints in ZIF-4 are much weaker than the angular constraints of silicate materials, leading to a less rigid network structure of ZIF-4 with a lower glass transition temperature.[53] As reported in Ref.[31], the radiolytic stability of MOFs is closely correlated with the strength of chemical interactions. In experiments, Zn-based MOFs have been found to exhibit collapse of the pore structure and densification after gamma irradiation, which is consistent with the present findings.

We then analyze the short-range structure of the ZIF-4 upon irradiation using a pair distribution function (PDF) analysis. To this end, the Zn-N and C-C partial PDFs have been calculated to highlight the local structure of Zn and imidazole ring. As shown in Figs. 3a and 3b, the Zn-N partial PDFs of crystalline and glassy ZIF-4 before irradiation mainly exhibit two peaks located at 2.22 and 4.36 Å, respectively. These correspond to the distances between Zn atoms and two N atoms in their neighboring imidazole rings (see Fig. 3e), respectively, with the peak intensities of crystalline ZIF-4 being much sharper than those in the glassy counterpart. Upon irradiation, the intensities of both peaks continuously decrease with an increase in the deposited energy, especially for the second peak which almost vanishes at an energy of 13.5 eV/atom. Both structures of ZIF-4 can be further amorphized to the same state, despite the initial differences in the structure of crystalline and glassy ZIF-4. The two peaks in C-C partial PDFs represent the directly (1.43 Å) and indirectly (2.20 Å) connected C atoms in the imidazole rings (see Figs. 3c, 3d and 3e). With an increase in the deposited energy, we also observe the emergence of a peak at 3.3 Å in the Zn-N PDF and one a 1.3 Å in the C-C PDF. The peak at 1.3 Å can be ascribed to C-C bonds in the broken imidazole rings. Since the peak at 3.3 Å is broad and not well-defined, we ascribe it to the Zn-N interaction between the first and second coordination shell of Zn due to the breakage of the imidazole ring. Indeed, both crystalline and

glassy ZIF-4 exhibit intact imidazole ring structures prior to irradiation, but with an increase in the deposited energy, the imidazole ring structures gradually decompose in both phases, which echoes the results shown in Fig. 2c. From the total pair distribution functions shown in Fig. S3 in the Supporting Information, we again observe both ZIF-4 phases converge to the same state upon irradiation.
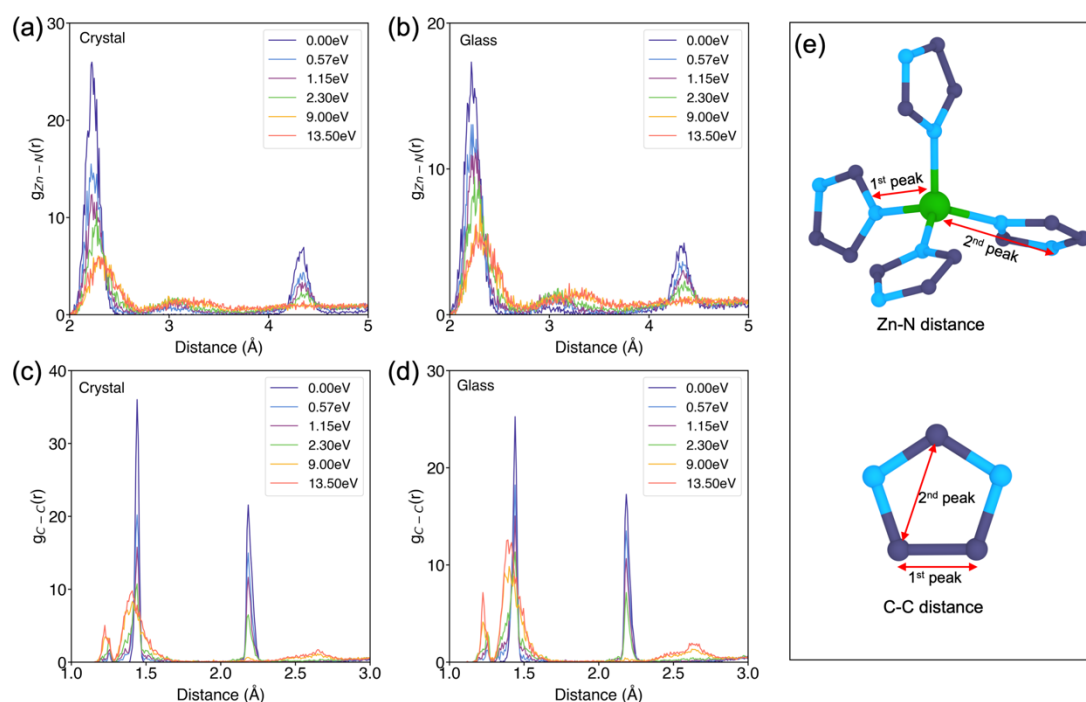
Fig. 3. (a,b) Zn-N partial pair distribution function of (a) ZIF-4 crystal and (b) glass under different doses of irradiation. (c,d) C-C partial pair distribution function of (c) ZIF-4 crystal and (d) glass under different doses of irradiation. (e) Schematics of the correlation between the peaks in the pair distribution function and the atomic structure. Zn, C, H and N are colored by green, grey, white, and light blue, respectively.

To further understand the effect of irradiation on the ZIF-4 structures, we have analyzed the pore structures and structure factor (Fig. 4) to characterize the changes in MRO upon irradiation. We find that the diffraction peaks of both phases become merged and shift toward larger Q values with an increase in the deposited energy (Figs. 4b-c), indicating that the structure becomes densified and more disordered upon irradiation. Interesting, despite the difference in the initial structure of the crystal and melt-quenched glass, both phases exhibit a similar structure regarding the structure factor when the deposited energy saturates, i.e., a similar first sharp diffraction peak (FSDP) located at around 2.0 Å^{-1} is observed when the sample is subjected to the irradiation energy of 13.5 eV/atom. The position evolution of FSDP during the irradiation process (Fig. S4) confirms that both phases densify to the same degree upon irradiation. Figures 4d and 4e show the pore size distribution of crystalline and glassy ZIF-4,

10

respectively, subjected to different amounts of irradiation energy upon irradiation. Initially, the pore sizes in crystalline ZIF-4 are larger than those in glassy ZIF-4, in agreement with previous findings [24]. With an increase in the deposited energy, the pore structures in both phases shift towards a lower diameter due to the collapse of internal pores in ZIF-4 upon irradiation. Consistent with the above-mentioned structural properties (i.e., density, CN of Zn, PDF, and S(Q)), we here also observe that the pore size distribution in both phases tends to be stabilized with a diameter of 2.6 Å when the energy saturates.
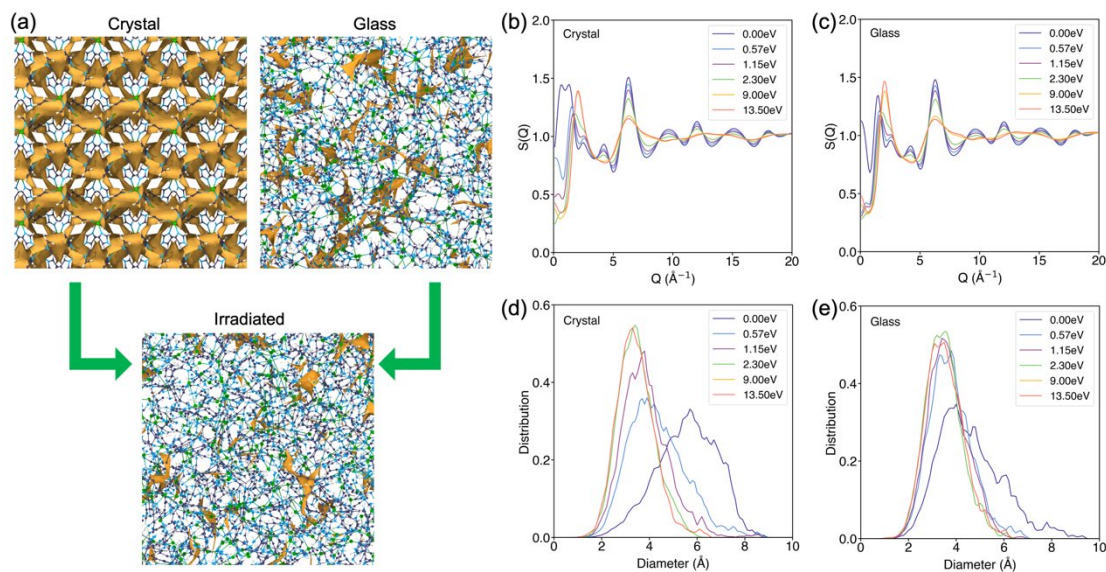
Fig. 4. (a) Illustration of the pore structure in the atomic structure of different ZIF-4 phases. The orange regions represent the free volumes. (b,c) Simulated neutron structure factor S(Q) of (b) ZIF-4 crystal and (c) glass subjected to different doses of irradiation. (d,e) Pore size distribution of (d) ZIF-4 crystal and (e) subjected to different doses of irradiation.

To better illustrate the hierarchical structural features across various scales, we have further investigated the ZIF-4 structures by persistent homology analysis following Refs.[39,48]. As shown in Figs. 5a-f, we observe that the distribution of the characteristic regions in the persistence diagrams (PDs) tends to fuse and get overlapped upon irradiation. Initially, both crystalline and glassy ZIF-4 exhibit three distinct regions, which correspond to different loop structures comprised of directly or indirectly connected atoms (see Fig. 5g). The region located at (0, 0.8) in the PD corresponds to the imidazole ring. In both ZIF-4 crystal and glass, this region becomes more diffuse upon irradiation, indicating the deformation and breakage of the imidazole ring. The horizontal distributed region with low birth values is attributed to chemically bonded loop structures. Since the death values in the PDs are closely correlated with the loop size, we clearly observe that the loop size decreases upon irradiation. We also note that the PDs are almost identical when the deposited energy saturates.
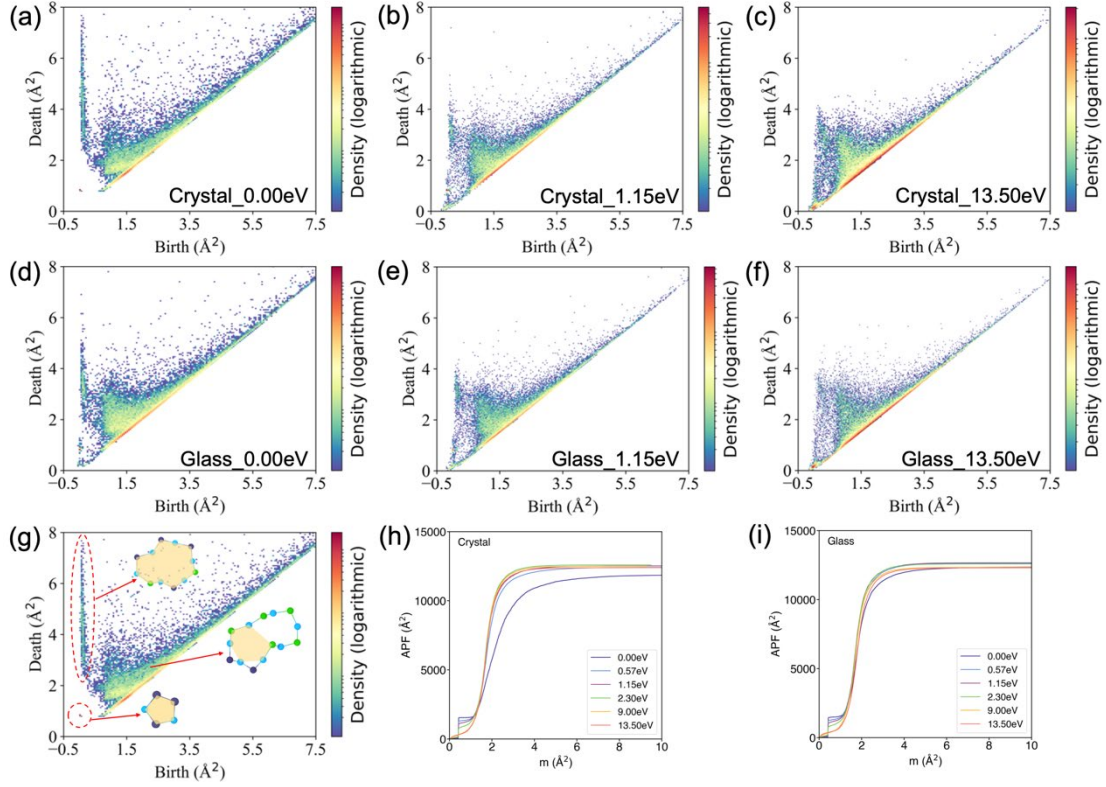
Fig. 5. (a-f) Persistence diagrams for (a-c) crystalline and (b-f) glassy ZIF-4 for initial (a, d) state and subjected to irradiation with dose of (b,e) 1.15 eV/atom, and (c,f) 13.5 eV/atom. (g) Schematics drawings of the loop structures corresponding to the different regions of the persistence diagram. (h,i) Quantitative analysis of persistence diagrams using the APF function for (h) crystalline and (i) glassy ZIF-4.

The accumulated persistence functions (APF) calculated based on the PDs are shown in Figs. 5h and 5i. The APF enables the quantitative comparison of PDs by calculating the cumulative sum up of all the points in the PDs weighted by their "lifetime" ($d_i - b_i$) as a function of the mean age ($m = (d_i + b_i)/2$), where d_i and b_i are the death and birth time of point i in the PD. Generally, all the APF curve increases and then feature at constant value at high m. For both crystalline and glassy ZIF-4, there is a small step at $m \sim 0.5$ Å^2, which gradually diminishes upon irradiation. This feature is due to imidazole rings, and therefore, this result also echoes the irradiation-induced decomposition of imidazole rings shown in Figs. 2c, 3c, and 3d. We also notice that an increased curve steepness at higher m upon irradiation, which is mainly due to a decreased mean age of the loops. Interestingly, the APF curves in both phases at the highest deposited energy become similar regarding the curve shape and absolute values (see Fig. S5).

To quantify the differences in structures modified by thermal treatment and irradiation, both the crystalline and glassy ZIF-4s are subjected to a reheating process at a rate of 1 K/ps to 1500 K. As expected, crystalline ZIF initially exhibits a lower potential energy than that of the glassy counterparts (see Fig. 6a). Upon heating, the divergence becomes less significant and finally

vanishes. We also notice that both phases start to evaporate when the temperature exceeds 1400 K. Next, we compare the potential energy and densify information during the heating process with that during the irradiation process. Figure 6b shows the different states of ZIF-4 under thermal or irradiation treatment in the potential energy-density space. Note that the ground-state potential energy is the potential energy of the inherent structure, which is achieved by performing an energy minimization while enforcing a zero pressure following the method from Ref.[54]. The points in Fig. 6b refer to the different configurations during the thermal or irradiation treatment processes. The glass structures under different cooling rates are obtained by quenching at 5, 10, 24, 50, and 100 K/ps, respectively. Generally, we observe that the "allowable" glasses (i.e., those that can be accessed via a thermal route) in the green region exhibit a relatively higher potential energy, which can be formed through the cooling of the melt. That is, irradiation leads to the formation of a more thermodynamically stable state. This phenomenon arises from the irradiation-induced densification of ZIF-4 phases and the decomposition of imidazole rings.
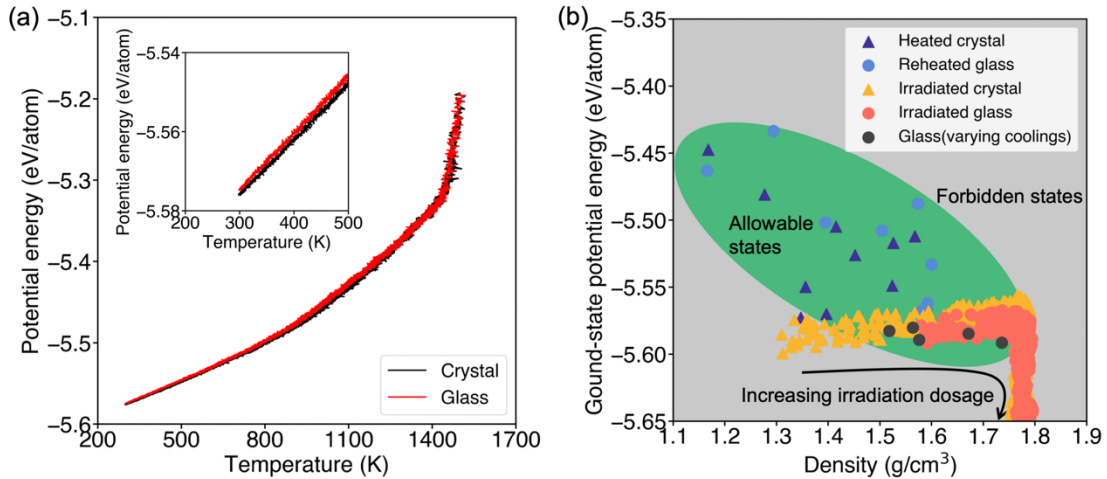
Fig. 6. (a) Potential energy evolution of crystalline and glassy ZIF-4 during the heating process as a function of temperature. The inset figure shows a magnification of the low temperature region. (b) Correlations between potential energy and density in different states of ZIF-4. The green region is a rough indication of the region of "allowable" states, whereas other regions are "forbidden" states.

We then analyze the mechanical properties of ZIF-4 in its "forbidden" states, i.e., subjected to different degrees of irradiation. Figures 7a and 7b show the simulated stress-strain curves of crystalline and glassy ZIF-4, respectively. The pristine state of both phases exhibits nanoductility as their fracture strain can reach a value up to 0.6, which agrees with previous findings[22]. The origin of nanoductility can be attributed to the bridging effect of the imidazole groups and the formation of nanocavities, which can effectively block the crack propagation. Consistent with the previous results, we also observe that the fracture of ZIF-4 is manifested

by the breakage of Zn-N coordination bonds, which are weaker than the covalent bonds in imidazole rings. With an increase in the deposited energy, the fracture strain gradually decreases from >0.6 to ~0.4 in both phases.
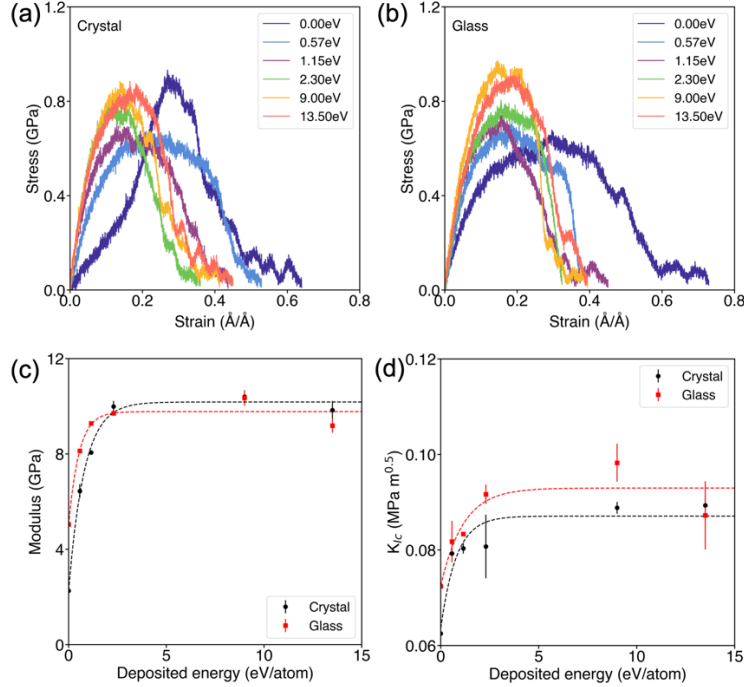

Fig. 7. (a,b) Stress-strain curves of (a) crystalline and (b) glassy ZIF-4 subjected to different doses of irradiation. (c,d) Computed Young's modulus (c) and fracture toughness (d) of crystalline and glassy ZIF-4 as a function of the deposited energy.

We then calculated the Young's modulus from the slope of a linear fit to the region of the strain-stress curve up to 5% strain. For oxide phases, typically the modulus will be decreased by irradiation[21,55,56]. However, here the modulus of both ZIF-4 phases increases and reach a constant value upon irradiation (Fig. 7c). Interestingly, although the modulus of glassy ZIF-4 is higher than the crystalline counterpart prior to irradiation, the difference in modulus between the two phases significantly decrease and eventually vanish (within the error range) upon irradiation. Since Young's modulus increases linearly with an increase in density for the present ZIF-4 system (see Fig. S6), the changes in modulus can be ascribed to the density variation induced by irradiation – this correlation also echoes experimental findings for different ZIF phases reported in Ref.[57]. The same is the case for fracture behavior. That is, although the fracture strain decreases upon irradiation, given the significant increase in Young's modulus, the fracture toughness (K_{Ic}) also exhibits an initial increase and then reaches a constant value upon irradiation (Fig. 7d). Therefore, from a mechanics point of view, irradiation can improve the stiffness as well as fracture toughness of ZIF-4 to a similar state despite the difference in initial structure. The "forbidden" irradiated state is therefore stiffer and tougher than the other

ZIF-4 states that can be accessed by a thermal route.

Figure 8a shows the tensile process of ZIF-4 glass with pre-crack prior to irradiation, highlighting blunting and propagation of the crack tip during the tensile process. With an increase in the applied strain, the width of the crack increases as bond breaking initiates. Before the sample is fully fractured, nanocavities can be observed in the same plane as the pre-crack within the bulk phase. Additional illustrations of the fracture process are shown in Fig. S7 (for crystalline ZIF-4) and Fig. S8 (for glassy ZIF-4). Furthermore, to better illustrate the fracture behavior influenced by irradiation, Figs. 8b-c and S9 show the magnified snapshots in the vicinity of the crack tip. We observe that the imidazole rings remain intact during the fracture (Fig. 8b), indicating that the crack propagation is attributed to the breakage of Zn-N bonds. The low fracture toughness of ZIF materials is therefore attributed to the relatively low energy of Zn-N coordination bonds[22]. For the irradiated glass with a deposited energy of 13.5 eV/atom, the decomposed imidazole rings have been transformed into atomic chains and these chains with covalent bonds can effectively impede the crack propagation process. This explains why the irradiated ZIF-4 state exhibits improved mechanical properties compared to the pristine state.
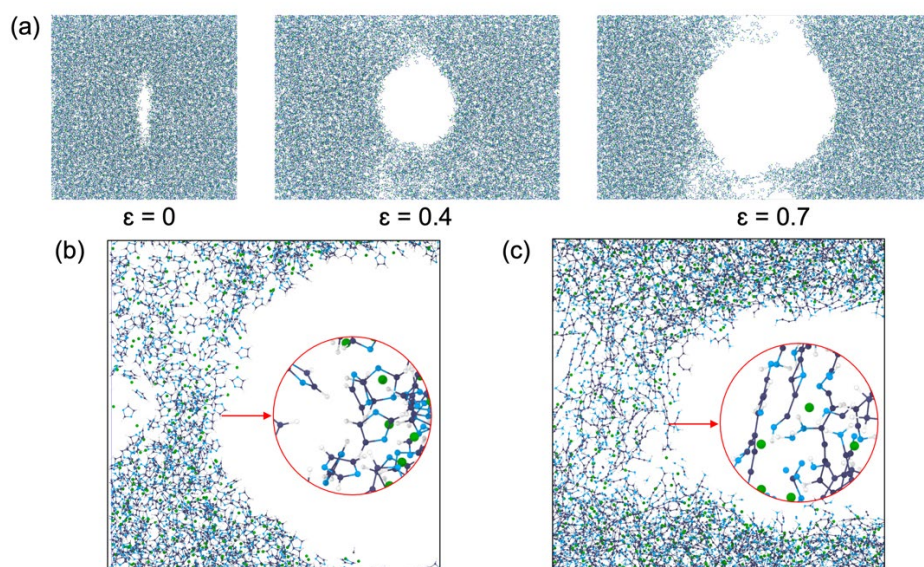
Fig. 8. (a) Evolution of fracture in the glassy ZIF-4 before irradiation at tensile strains of 0.0, 0.4, and 0.7. (b,c) Atomic snapshot at the vicinity of the crack tip in the ZIF-4 glasses (b) before and (c) after irradiation at the dose of 13.5 eV/atom.

4. Conclusions

We have studied the structure and mechanical properties of crystalline and glassy ZIF-4 under different irradiation treatments through reactive MD simulations. For both phases of ZIF-4, the

structure changes induced by irradiation are attributed to the decomposition of imidazole rings, which enables the structure to access a "forbidden" disordered state that is not accessible through thermal treatments. Despite the differences in the initial structure of crystalline vs. glassy ZIF-4, both the short- and medium-range order structure of the irradiated ZIF-4 structures tend to converge to the same disordered state with an increase in the deposited energy, with simultaneous changes in the mechanical properties. Importantly, we observed that the irradiated ZIF-4 state exhibits a higher Young's modulus and fracture toughness compared to the pristine structures. The strengthening mechanism can be attributed to the decomposed imidazole rings that act as reinforcement by hindering the plastic deformation and crack propagation in the materials.

Acknowledgements

Supporting Information

The Supporting Information associated with this article can be found on the website of DOI:XXX.

Pair distribution functions of ZIF-4 in the crystalline, liquid, and glassy states. Potential energy, total pair distribution function, and accumulated persistence function of both ZIF-4 crystal and glass influenced by irradiation. Atomic snapshots of both ZIF-4 crystal and glass during fracture.

Conflicts of interest

The authors declare no competing interests.

References

(1) Wu, T.; Feng, X.; Elsaidi, S. K.; Thallapally, P. K.; Carreon, M. A. Zeolitic Imidazolate Framework-8 (ZIF-8) Membranes for Kr/Xe Separation. *Ind. Eng. Chem. Res.* **2017**, *56* (6), 1682–1686. https://doi.org/10.1021/acs.iecr.6b04868.

(2) Su, Z.; Shaw, W. L.; Miao, Y.-R.; You, S.; Dlott, D. D.; Suslick, K. S. Shock Wave Chemistry in a Metal–Organic Framework. *J. Am. Chem. Soc.* **2017**, *139* (13), 4619–4622. https://doi.org/10.1021/jacs.6b12956.

(3) Mondloch, J. E.; Katz, M. J.; Isley III, W. C.; Ghosh, P.; Liao, P.; Bury, W.; Wagner, G. W.; Hall, M. G.; DeCoste, J. B.; Peterson, G. W.; Snurr, R. Q.; Cramer, C. J.; Hupp, J. T.; Farha, O. K. Destruction of Chemical Warfare Agents Using Metal–Organic Frameworks. *Nat. Mater.* **2015**, *14* (5), 512–516. https://doi.org/10.1038/nmat4238.

(4) Horike, S.; Umeyama, D.; Kitagawa, S. Ion Conductivity and Transport by Porous Coordination Polymers and Metal–Organic Frameworks. *Accounts Chem. Res.* **2013**, *46* (11), 2376–2384. https://doi.org/10.1021/ar300291s.

(5) Qiao, A.; Bennett, T. D.; Tao, H.; Krajnc, A.; Mali, G.; Doherty, C. M.; Thornton, A. W.; Mauro, J. C.; Greaves, G. N.; Yue, Y. A Metal-Organic Framework with Ultrahigh Glass-Forming Ability. *Sci. Adv.* **2018**, *4* (3), eaao6827. https://doi.org/10.1126/sciadv.aao6827.

(6) Madsen, R. S. K.; Qiao, A.; Sen, J.; Hung, I.; Chen, K.; Gan, Z.; Sen, S.; Yue, Y. Ultrahigh-Field ^{67} Zn NMR Reveals Short-Range Disorder in Zeolitic Imidazolate Framework Glasses. *Science* **2020**, *367* (6485), 1473–1476. https://doi.org/10.1126/science.aaz0251.

(7) Qiao, A.; Tao, H.; Carson, M. P.; Aldrich, S. W.; Thirion, L. M.; Bennett, T. D.; Mauro, J. C.; Yue, Y. Optical Properties of a Melt-Quenched Metal–Organic Framework Glass. *Opt. Lett.* **2019**, *44* (7), 1623–1625. https://doi.org/10.1364/OL.44.001623.

(8) Ali, Mohamed. A.; Ren, J.; Zhao, T.; Liu, X.; Hua, Y.; Yue, Y.; Qiu, J. Broad Mid-Infrared Luminescence in a Metal–Organic Framework Glass. *ACS Omega* **2019**, *4* (7), 12081–12087. https://doi.org/10.1021/acsomega.9b01559.

(9) Tan, J. C.; Bennett, T. D.; Cheetham, A. K. Chemical Structure, Network Topology, and Porosity Effects on the Mechanical Properties of Zeolitic Imidazolate Frameworks. *Proc. Natl. Acad. Sci. U.S.A.* **2010**, *107* (22), 9938–9943. https://doi.org/10.1073/pnas.1003205107.

(10) Zhou, C.; Longley, L.; Krajnc, A.; Smales, G. J.; Qiao, A.; Erucar, I.; Doherty, C. M.; Thornton, A. W.; Hill, A. J.; Ashling, C. W.; Qazvini, O. T.; Lee, S. J.; Chater, P. A.; Terrill, N. J.; Smith, A. J.; Yue, Y.; Mali, G.; Keen, D. A.; Telfer, S. G.; Bennett, T. D. Metal-Organic Framework Glasses with Permanent Accessible Porosity. *Nat. Commun.* **2018**, *9* (1), 5042. https://doi.org/10.1038/s41467-018-07532-z.

(11) Phan, A.; Doonan, C. J.; Uribe-Romo, F. J.; Knobler, C. B.; O'Keeffe, M.; Yaghi, O. M. Synthesis, Structure, and Carbon Dioxide Capture Properties of Zeolitic Imidazolate Frameworks. *Accounts Chem. Res.* **2010**, *43* (1), 58–67. https://doi.org/10.1021/ar900116g.

(12) Bennett, T. D.; Tan, J.-C.; Yue, Y.; Baxter, E.; Ducati, C.; Terrill, N. J.; Yeung, H. H.-M.; Zhou, Z.; Chen, W.; Henke, S.; Cheetham, A. K.; Greaves, G. N. Hybrid Glasses from Strong and Fragile Metal-Organic Framework Liquids. *Nat. Commun.* **2015**, *6* (1), 8079. https://doi.org/10.1038/ncomms9079.

(13) Gaillac, R.; Pullumbi, P.; Coudert, F.-X. Melting of Zeolitic Imidazolate Frameworks with Different Topologies: Insight from First-Principles Molecular Dynamics. *J. Phys. Chem. C* **2018**, *122* (12), 6730–6736. https://doi.org/10.1021/acs.jpcc.8b00385.

(14) Bennett, T. D.; Yue, Y.; Li, P.; Qiao, A.; Tao, H.; Greaves, N. G.; Richards, T.; Lampronti, G. I.; Redfern, S. A. T.; Blanc, F.; Farha, O. K.; Hupp, J. T.; Cheetham, A. K.; Keen, D. A. Melt-Quenched Glasses of Metal–Organic Frameworks. *J. Am. Chem. Soc.* **2016**, *138* (10), 3484–3492. https://doi.org/10.1021/jacs.5b13220.

(15) Bennett, T. D.; Simoncic, P.; Moggach, S. A.; Gozzo, F.; Macchi, P.; Keen, D.

A.; Tan, J.-C.; Cheetham, A. K. Reversible Pressure-Induced Amorphization of a Zeolitic Imidazolate Framework (ZIF-4). *Chem. Commun.* **2011**, *47* (28), 7983–7985. https://doi.org/10.1039/C1CC11985K.

(16) Cao, S.; Bennett, T. D.; Keen, D. A.; Goodwin, A. L.; Cheetham, A. K. Amorphization of the Prototypical Zeolitic Imidazolate Framework ZIF-8 by Ball-Milling. *Chem. Commun.* **2012**, *48* (63), 7805. https://doi.org/10.1039/c2cc33773h.

(17) Gupta, P. K. Non-Crystalline Solids: Glasses and Amorphous Solids. *J. Non-Cryst. Solids* **1996**, *195* (1), 158–164. https://doi.org/10.1016/0022-3093(95)00502-1.

(18) Varshneya, A. K. *Fundamentals of Inorganic Glasses*; Elsevier, 2013.

(19) Krishnan, N. M. A.; Wang, B.; Yu, Y.; Le Pape, Y.; Sant, G.; Bauchy, M. Enthalpy Landscape Dictates the Irradiation-Induced Disordering of Quartz. *Phys. Rev. X* **2017**, *7* (3), 031019. https://doi.org/10.1103/PhysRevX.7.031019.

(20) Krishnan, N. M. A.; Wang, B.; Le Pape, Y.; Sant, G.; Bauchy, M. Irradiation-Driven Amorphous-to-Glassy Transition in Quartz: The Crucial Role of the Medium-Range Order in Crystallization. *Phys. Rev. Materials* **2017**, *1* (5), 053405. https://doi.org/10.1103/PhysRevMaterials.1.053405.

(21) Ravinder, R.; Kumar, A.; Kumar, R.; Vangla, P.; Krishnan, N. M. A. Irradiation-Induced Brittle-to-Ductile Transition in α-Quartz. *J. Am. Ceram. Soc.* **2020**, *103* (7), 3962–3970. https://doi.org/10.1111/jace.16951.

(22) To, T.; Sørensen, S. S.; Stepniewska, M.; Qiao, A.; Jensen, L. R.; Bauchy, M.; Yue, Y.; Smedskjaer, M. M. Fracture Toughness of a Metal–Organic Framework Glass. *Nat. Commun.* **2020**, *11* (1), 2593. https://doi.org/10.1038/s41467-020-16382-7.

(23) Stukowski, A. Visualization and Analysis of Atomistic Simulation Data with OVITO–the Open Visualization Tool. *Model. Simul. Mater. Sci. Eng.* **2009**, *18* (1), 015012. https://doi.org/10.1088/0965-0393/18/1/015012.

(24) Yang, Y.; Shin, Y. K.; Li, S.; Bennett, T. D.; van Duin, A. C. T.; Mauro, J. C. Enabling Computational Design of ZIFs Using ReaxFF. *J. Phys. Chem. B* **2018**, *122* (41), 9616–9624. https://doi.org/10.1021/acs.jpcb.8b08094.

(25) Sørensen, S. S.; Østergaard, M. B.; Stepniewska, M.; Johra, H.; Yue, Y.; Smedskjaer, M. M. Metal–Organic Framework Glasses Possess Higher Thermal Conductivity than Their Crystalline Counterparts. *ACS Appl. Mater. Interfaces* **2020**, *12* (16), 18893–18903. https://doi.org/10.1021/acsami.0c02310.

(26) Allen, F. H. The Cambridge Structural Database: A Quarter of a Million Crystal Structures and Rising. *Acta Cryst. B* **2002**, *58* (3), 380–388. https://doi.org/10.1107/S0108768102003890.

(27) Berendsen, H. J. C.; Postma, J. P. M.; van Gunsteren, W. F.; DiNola, A.; Haak, J. R. Molecular Dynamics with Coupling to an External Bath. *J. Chem. Phys.* **1984**, *81* (8), 3684–3690. https://doi.org/10.1063/1.448118.

(28) Nosé, S. A Molecular Dynamics Method for Simulations in the Canonical Ensemble. *Mol. Phys.* **1984**, *52* (2), 255–268. https://doi.org/10.1080/00268978400101201.

(29) Krishnan, N. M. A.; Ravinder, R.; Kumar, R.; Le Pape, Y.; Sant, G.; Bauchy, M. Density–Stiffness Scaling in Minerals upon Disordering: Irradiation vs. Vitrification.

Acta Mater. **2019**, *166*, 611–617. https://doi.org/10.1016/j.actamat.2019.01.015.

(30) Reghioua, I.; Lancry, M.; Cavani, O.; Floch, S. L.; Neuville, D. R.; Ollier, N. Unique Silica Polymorph Obtained under Electron Irradiation. *Appl. Phys. Lett.* **2019**, *115* (25), 251101. https://doi.org/10.1063/1.5127836.

(31) Volkringer, C.; Falaise, C.; Devaux, P.; Giovine, R.; Stevenson, V.; Pourpoint, F.; Lafon, O.; Osmond, M.; Jeanjacques, C.; Marcillaud, B.; Sabroux, J. C.; Loiseau, T. Stability of Metal–Organic Frameworks under Gamma Irradiation. *Chem. Commun.* **2016**, *52* (84), 12502–12505. https://doi.org/10.1039/C6CC06878B.

(32) Faber, T. E.; Ziman, J. M. A Theory of the Electrical Properties of Liquid Metals. *Philos. Mag.* **1965**, *11* (109), 153–173. https://doi.org/10.1080/14786436508211931.

(33) Zhou, Q.; Shi, Y.; Deng, B.; Du, T.; Guo, L.; Smedskjaer, M. M.; Bauchy, M. Revealing the Medium-Range Structure of Glassy Silica Using Force-Enhanced Atomic Refinement. *Journal of Non-Crystalline Solids* **2021**, *573*, 121138. https://doi.org/10.1016/j.jnoncrysol.2021.121138.

(34) Willems, T. F.; Rycroft, C. H.; Kazi, M.; Meza, J. C.; Haranczyk, M. Algorithms and Tools for High-Throughput Geometry-Based Analysis of Crystalline Porous Materials. *Microporous Mesoporous Mat.* **2012**, *149* (1), 134–141. https://doi.org/10.1016/j.micromeso.2011.08.020.

(35) Pinheiro, M.; Martin, R. L.; Rycroft, C. H.; Jones, A.; Iglesia, E.; Haranczyk, M. Characterization and Comparison of Pore Landscapes in Crystalline Porous Materials. *J. Mol. Graph.* **2013**, *44*, 208–219. https://doi.org/10.1016/j.jmgm.2013.05.007.

(36) Gaillac, R.; Pullumbi, P.; Bennett, T. D.; Coudert, F.-X. Structure of Metal–Organic Framework Glasses by Ab Initio Molecular Dynamics. *Chem. Mater.* **2020**, *32* (18), 8004–8011. https://doi.org/10.1021/acs.chemmater.0c02950.

(37) Gaillac, R.; Pullumbi, P.; Beyer, K. A.; Chapman, K. W.; Keen, D. A.; Bennett, T. D.; Coudert, F.-X. Liquid Metal–Organic Frameworks. *Nat. Mater.* **2017**, *16* (11), 1149–1154. https://doi.org/10.1038/nmat4998.

(38) Le Roux, S.; Jund, P. Ring Statistics Analysis of Topological Networks: New Approach and Application to Amorphous GeS2 and SiO2 Systems. *Comput. Mater. Sci.* **2010**, *49* (1), 70–83. https://doi.org/10.1016/j.commatsci.2010.04.023.

(39) Hiraoka, Y.; Nakamura, T.; Hirata, A.; Escolar, E. G.; Matsue, K.; Nishiura, Y. Hierarchical Structures of Amorphous Solids Characterized by Persistent Homology. *Proc. Natl. Acad. Sci. U.S.A.* **2016**, *113* (26), 7035–7040. https://doi.org/10.1073/pnas.1520877113.

(40) Saadatfar, M.; Takeuchi, H.; Robins, V.; Francois, N.; Hiraoka, Y. Pore Configuration Landscape of Granular Crystallization. *Nat. Commun.* **2017**, *8* (1), 15082. https://doi.org/10.1038/ncomms15082.

(41) Tanaka, H.; Tong, H.; Shi, R.; Russo, J. Revealing Key Structural Features Hidden in Liquids and Glasses. *Nat. Rev. Phys.* **2019**, *1* (5), 333–348. https://doi.org/10.1038/s42254-019-0053-3.

(42) Onodera, Y.; Kohara, S.; Tahara, S.; Masuno, A.; Inoue, H.; Shiga, M.; Hirata, A.; Tsuchiya, K.; Hiraoka, Y.; Obayashi, I.; Ohara, K.; Mizuno, A.; Sakata, O. Understanding Diffraction Patterns of Glassy, Liquid and Amorphous Materials via Persistent Homology Analyses. *J. Ceram. Soc. Jpn.* **2019**, *127* (12), 853–863.

https://doi.org/10.2109/jcersj2.19143.

(43) Onodera, Y.; Kohara, S.; Salmon, P. S.; Hirata, A.; Nishiyama, N.; Kitani, S.; Zeidler, A.; Shiga, M.; Masuno, A.; Inoue, H.; Tahara, S.; Polidori, A.; Fischer, H. E.; Mori, T.; Kojima, S.; Kawaji, H.; Kolesnikov, A. I.; Stone, M. B.; Tucker, M. G.; McDonnell, M. T.; Hannon, A. C.; Hiraoka, Y.; Obayashi, I.; Nakamura, T.; Akola, J.; Fujii, Y.; Ohara, K.; Taniguchi, T.; Sakata, O. Structure and Properties of Densified Silica Glass: Characterizing the Order within Disorder. *NPG Asia Mater* **2020**, *12* (1), 85. https://doi.org/10.1038/s41427-020-00262-z.

(44) Hosokawa, S.; Bérar, J.-F.; Boudet, N.; Pilgrim, W.-C.; Pusztai, L.; Hiroi, S.; Maruyama, K.; Kohara, S.; Kato, H.; Fischer, H. E.; Zeidler, A. Partial Structure Investigation of the Traditional Bulk Metallic Glass Pd 40 Ni 40 P 20. *Phys. Rev. B* **2019**, *100* (5), 054204. https://doi.org/10.1103/PhysRevB.100.054204.

(45) Onodera, Y.; Takimoto, Y.; Hijiya, H.; Taniguchi, T.; Urata, S.; Inaba, S.; Fujita, S.; Obayashi, I.; Hiraoka, Y.; Kohara, S. Origin of the Mixed Alkali Effect in Silicate Glass. *NPG Asia Mater* **2019**, *11* (1), 1–11. https://doi.org/10.1038/s41427-019-0180-4.

(46) Dmitriy. Diode—Persistent Homology Software, 2021.

(47) Dmitriy. Dionysus2—Persistent Homology Software, 2021.

(48) Sørensen, S. S.; Biscio, C. A. N.; Bauchy, M.; Fajstrup, L.; Smedskjaer, M. M. Revealing Hidden Medium-Range Order in Amorphous Materials Using Topological Data Analysis. *Sci. Adv.* **2020**, *6* (37), eabc2320. https://doi.org/10.1126/sciadv.abc2320.

(49) Brochard, L.; Hantal, G.; Laubie, H.; Ulm, F. J.; Pellenq, R. J.-M. Fracture Mechanisms in Organic-Rich Shales: Role of Kerogen. *Poromechanics V (ASCE, 2013)* **2013**, 2471–2480. https://doi.org/10.1061/9780784412992.288.

(50) Bauchy, M.; Laubie, H.; Abdolhosseini Qomi, M. J.; Hoover, C. G.; Ulm, F.-J.; Pellenq, R. J.-M. Fracture Toughness of Calcium–Silicate–Hydrate from Molecular Dynamics Simulations. *J. Non-Cryst. Solids* **2015**, *419*, 58–64. https://doi.org/10.1016/j.jnoncrysol.2015.03.031.

(51) Bauchy, M.; Wang, B.; Wang, M.; Yu, Y.; Abdolhosseini Qomi, M. J.; Smedskjaer, M. M.; Bichara, C.; Ulm, F.-J.; Pellenq, R. Fracture Toughness Anomalies: Viewpoint of Topological Constraint Theory. *Acta Mater.* **2016**, *121*, 234–239. https://doi.org/10.1016/j.actamat.2016.09.004.

(52) Du, T.; Blum, M.; Chen, C.; Muraleedharan, M. G.; van Duin, A. C. T.; Newell, P. Nanomechanical Investigation of the Interplay between Pore Morphology and Crack Orientation of Amorphous Silica. *Eng. Fract. Mech.* **2021**, *250*, 107749. https://doi.org/10.1016/j.engfracmech.2021.107749.

(53) Yang, Y.; Wilkinson, C. J.; Lee, K.-H.; Doss, K.; Bennett, T. D.; Shin, Y. K.; van Duin, A. C. T.; Mauro, J. C. Prediction of the Glass Transition Temperatures of Zeolitic Imidazolate Glasses through Topological Constraint Theory. *J. Phys. Chem. Lett.* **2018**, *9* (24), 6985–6990. https://doi.org/10.1021/acs.jpclett.8b03348.

(54) Parrinello, M.; Rahman, A. Polymorphic Transitions in Single Crystals: A New Molecular Dynamics Method. *J. Appl. Phys.* **1998**, *52* (12), 7182. https://doi.org/10.1063/1.328693.

(55) Krishnan, N. M. A.; Le Pape, Y.; Sant, G.; Bauchy, M. Effect of Irradiation on Silicate Aggregates' Density and Stiffness. *J. Nucl. Mater.* **2018**, *512*, 126–136. https://doi.org/10.1016/j.jnucmat.2018.10.009.

(56) Ren, X.; Du, T.; Peng, H.; Jensen, L. R.; Biscio, C. A. N.; Fajstrup, L.; Bauchy, M.; Smedskjaer, M. M. Irradiation-Induced Toughening of Calcium Aluminoborosilicate Glasses. *Materials Today Communications* **2022**, *31*, 103649. https://doi.org/10.1016/j.mtcomm.2022.103649.

(57) Bennett, T. D.; Yue, Y.; Li, P.; Qiao, A.; Tao, H.; Greaves, N. G.; Richards, T.; Lampronti, G. I.; Redfern, S. A. T.; Blanc, F.; Farha, O. K.; Hupp, J. T.; Cheetham, A. K.; Keen, D. A. Melt-Quenched Glasses of Metal–Organic Frameworks. *J. Am. Chem. Soc.* **2016**, *138* (10), 3484–3492. https://doi.org/10.1021/jacs.5b13220.

TOC graphic

ZIF-4 crystal

ZIF-4 glass

vitrification

Irradiation

Irradiated ZIF-4